

Temporal and spatial properties of fluctuations below a supercritical primary bifurcation to traveling oblique-roll electroconvection

Michael A. Scherer and Guenter Ahlers

Department of Physics and iQUEST, University of California, Santa Barbara, California 93106

(Received 3 December 2001; published 26 April 2002)

We present measurements of thermally-induced oblique-roll traveling-wave (TW) fluctuations below the supercritical primary bifurcation to electroconvection (EC) in the nematic liquid crystal 4-ethyl-2-fluoro-4'-[2-(trans-4-pentylcyclohexyl)ethyl]-biphenyl (I52). First we analyze time sequences of one-dimensional shadowgraph images taken parallel to the director to obtain the TW frequency ω and the fluctuation lifetime τ . Within our resolution we find that ω is independent of $\epsilon \equiv V/V_c - 1$ (V is the applied voltage amplitude and V_c its value at the onset of convection). Contrary to linear theory, the relaxation rate $1/\tau$ remains finite at the bifurcation. Next we present the analysis of temporally uncorrelated two-dimensional shadowgraph images of the fluctuations for several values of the electrical conductivity σ . We fitted an anisotropic two-dimensional Lorentzian function, corresponding to oblique-roll EC, to the time-averaged structure factors $S(\mathbf{k})$ derived from the images. This yielded information about the components of the mean wave vector \mathbf{k}_0 and about the correlation length ξ as a function of σ and ϵ . The angle of obliqueness ϑ of the roll patterns was independent of σ but decreased anomalously as ϵ approached zero. The modulus k_0 of \mathbf{k}_0 depended on σ . It also showed an anomalous reduction close to onset. The anomalous ϵ dependence of k_0 and ϑ disagrees with linear theory, which predicts a smooth, essentially linear dependence on ϵ , and presumably is caused by nonlinear interactions between the fluctuations.

DOI: 10.1103/PhysRevE.65.051101

PACS number(s): 05.40.-a, 64.60.Fr

I. INTRODUCTION

Pattern formation is common in our daily life: The development of vortices while mixing coffee and milk in a cup, the formation of sand ripples on the beach by wind or water, or the buildup of clouds in the sky by rising hot, humid air present just a few examples [1]. There is even evidence that pattern formation played a significant role in the early universe, in the preheating stage at the end of inflation when explosive particles were produced [2]. Common aspects of pattern-forming systems are that they are dissipative and driven far from equilibrium. The appearance of the same patterns such as stripes, squares, hexagons, or spirals in diverse systems suggests an underlying universality of the phenomenon. During the last two decades much work has been devoted to understanding the governing principles of pattern formation by using systems based on, e.g., reaction-diffusion processes, solidification, vertically vibrated layers of sand, or fluid flow [3].

Even below the bifurcation to patterns there already exist fluctuations away from the spatially uniform state. These are driven by external noise, which under carefully controlled experimental conditions can be dominated by the thermal noise associated with the Brownian motion of the atoms or molecules. When the control parameter is raised above the critical value, patterns often evolve from inhomogeneities of the experimental system; but when these inhomogeneities are kept at a negligible level, the structures will grow from fluctuations [4]. In the present paper we present experimental results for the properties of fluctuations below the onset of pattern formation in one particular system, namely, electroconvection (EC) in a nematic liquid crystal (NLC). Indeed, the first quantitative experimental study of fluctuations in a

hydrodynamic system of which we are aware was done using EC of a NLC [5]; but for this system there is as yet no quantitative theory and only semiquantitative general arguments about the influence of $k_B T$ could be used for comparison. This comparison yielded good agreement for the root-mean-square (rms) fluctuation amplitudes at a semiquantitative level.

Rayleigh-Bénard convection (RBC) has been used most extensively for the study of pattern formation [3,6]. Here a horizontal fluid layer, confined at the bottom and top, is heated from below. When the temperature difference exceeds a threshold, the system undergoes a sharp bifurcation from a uniform state to a state where patterns occur. The steady-state pattern amplitude grows continuously beyond the transition, i.e., the bifurcation is supercritical. Below the bifurcation there exist fluctuations δT of the temperature field which are induced by thermal noise. Near the bifurcation point the fluctuations become "large" in the sense that linear theory (LT) predicts that they diverge [7]; but in practice they remain quite small and difficult to measure. The fluctuation amplitudes have zero mean but a finite mean square $\langle \delta T^2 \rangle$. Predictions of $\langle \delta T^2 \rangle$ were already made three decades ago [8–12] on the basis of LT, and a quantitative evaluation based on linear Landau fluctuating hydrodynamics [13] was provided by van Beijeren and Cohen [14]. Very recently Ortiz de Zárate and Sengers calculated the entire structure factor $S(k_0)$ of δT in the linear approximation (k_0 is the wave number of the fluctuation) [15]. The integral of $S(k_0)$ yields $\langle \delta T^2 \rangle$ and recovers the earlier result near the onset of convection [14]. Since $\langle \delta T^2 \rangle$ is extremely small, quantitative experimental verification could be obtained only much more recently. Quentin and Rehberg [16] measured the amplitudes of fluctuating patterns in a laterally confined (i.e.,

pseudo-one-dimensional) binary mixture of water and ethanol and found good agreement with a theoretical prediction; but the theory does not take the influence of mixture effects and of the near sidewalls quantitatively into account. At about the same time Wu *et al.* [17] reported quantitative measurements of rms fluctuation amplitudes for a RBC system extended in two dimensions using compressed CO₂ as the fluid; these results agreed quantitatively with the calculations of van Beijeren and Cohen [18] which, given linear Landau fluctuating hydrodynamics [13] as a starting point, are the exact linear results for a two-dimensional laterally infinite system.

Sufficiently close to the bifurcation fluctuation amplitudes become so large that one expects interactions between the fluctuations due to the nonlinear terms in the deterministic equations of motion. In this parameter range LT should break down. In analogy with critical phenomena in equilibrium systems, one then expects a modified “critical” (rather than “mean field”) behavior of the system. For RBC it was predicted by Swift and Hohenberg [11,12] that the fluctuation interactions should lead to a first-order transition, i.e., to a subcritical bifurcation. Experimentally this interesting phenomenon has been out of reach so far because under most circumstances it is expected to become noticeable only within a few parts per million of the bifurcation point [11,12,19].

A more favorable system to study the influence of thermal noise, and in particular of nonlinear effects, is EC in a NLC [20]. In the class of EC systems considered here the NLC is confined between parallel glass plates with a spacing typically in the range of 10 to 100 μm between them, and the director of the NLC is aligned in a unique direction parallel to the plates (“planar” alignment). On their inside the glass plates are covered with transparent electrodes, and an alternating voltage of amplitude V is applied to the cell. The role of the temperature difference is now taken by V , and EC occurs for $V > V_c$. The pattern that forms can consist of rolls with their axes orthogonal to the director (normal rolls), or the axes can be oriented at some other angle (oblique rolls). The effects of thermal noise are larger than for RBC for two reasons. First, the effective noise intensity [5] $F = k_B T / E$ is large because the relevant dissipative energy $E = d \langle \bar{k} \rangle$ of the system involves a combination of elastic constants $\langle \bar{k} \rangle$ which is an order of magnitude smaller than the typical corresponding term $\rho \nu^2$ for RBC (here ρ is the density and ν the kinematic viscosity of the fluid). This large susceptibility to external noise was recognized long ago by Graham [10]. Second, the effect of this intrinsically large susceptibility is supplemented by the very small thickness d of the cells used in EC, which (compared to RBC) enhances F by yet another order of magnitude. As mentioned above, it was shown already a decade ago that it was possible to visualize the fluctuating convective patches and to measure their amplitudes below onset by using the NLC N-(p-methoxybenzylidene)-p-butylaniline (MBBA) [5]. Consistency with semiquantitative considerations based on LT was found. These findings have been confirmed more recently by additional measurements using “Merck Phase V” (MPV) [21] and 4-ethyl-2-fluoro-

4'-[2-(trans-4-pentylcyclohexyl)ethyl]-bi-phenyl [22–24]. (152)

Recently, it was shown experimentally [24] that there are deviations from LT of the fluctuation amplitudes below the supercritical primary bifurcation to EC. The mean-square director-angle fluctuations $\langle \theta^2 \rangle$ were measured for the two different NLCs MPV and I52. For $\epsilon_{mf} \equiv V^2 / V_{c, mf}^2 - 1 \leq -0.1$ it was found that $\langle \theta^2 \rangle \propto |\epsilon_{mf}|^{-\gamma}$ with γ given by LT. Closer to the bifurcation a smaller exponent γ and a shifted onset $V_c^2 > V_{c, mf}^2$ were found. A detailed nonlinear theory for this system is not available. Its critical behavior need not be the same as that of RBC because the anisotropy of the NLC suggests that it may belong to a different universality class.

For the work presented in this paper we used the NLC I52. EC in I52 exhibits a large variety of different patterns [26] which are determined by the electrical conductivity and by the frequency of the applied voltage. They range from localized structures (so-called “worms”) at low conductivities [27] to spatiotemporal chaos at intermediate conductivities [28]. At even higher conductivities the patterns remain stationary. In this work we deal with the intermediate regime where oblique rolls bifurcate supercritically from the conduction state. The degenerate *zig* and *zag* rolls, which make angles ϑ and $-\vartheta$ with the director, consist of traveling waves (TWs). Interaction between the *zig* and *zag* right- and left-traveling waves leads to spatiotemporal chaos immediately above the onset of EC [28].

In spite of its complexity, pattern formation in EC is remarkably well understood theoretically and overall agreement with the very rich experimental observations is excellent. Bodenschatz *et al.* [25] gave a theoretical description of the threshold and near-threshold behavior of what is now known as the standard model (SM) of electroconvection. Based on the hydrodynamic equations they derived a Ginzburg-Landau equation for the amplitude A of the hydrodynamic fields, expected to be valid near threshold [29], which for the case of oblique rolls [see Eq. (5.13) in [25]] is given by

$$\tau_0 \delta_t A = [\xi_x^2 \delta_x^2 + \xi_y^2 \delta_y^2 + \xi_{xy}^2 \delta_x \delta_y + \epsilon - |A|^2] A. \quad (1)$$

Here $\epsilon \equiv V^2 / V_c^2 - 1$ and $\xi_n, n = x, y, xy$ are the components of the correlation length ξ . In the linear regime below onset we may neglect the nonlinear term, and expect the fluctuations to be determined by a stochastic version of this equation.

Comparison with several experiments revealed that the SM provided good estimates of the voltage V_c at the onset of convection and of the initial wave number k_c of the pattern. However, it failed to predict the Hopf bifurcation to TWs and the subcritical nature of the bifurcation which were observed over some parameter ranges [5,30–36]. This motivated Treiber and Kramer [37] to extend the SM by introducing a weak-electrolyte model (WEM). The WEM includes the dissociation-recombination reaction of the ionic dopant in the sample. It correctly predicts the Hopf bifurcation to TWs in good agreement with experiments in I52 [38] and MPV [39]. It yields a Ginzburg-Landau equation like Eq. (1), but the correlation-length components ξ_n are supplemented by additive imaginary terms.

In previous work a one-dimensional Lorentzian function was fitted to an azimuthal average of the experimental structure-factor data. For thermal fluctuations in I52 (see Refs. [22–24]) a good fit was obtained (see Fig. 3 in Ref. [23]) even though the system does not have the rotational symmetry that would justify an azimuthal average. The analysis yielded an average wave number and correlation length. In the present paper we extend the analysis of the

thermal fluctuations in Fourier space and present a two-dimensional analysis of the Fourier peaks using the two-dimensional structure factor L corresponding to Eq. (1) [29]. Since the data are time averaged and contain no frequency information, we used the integral of $L(\mathbf{k}, \tilde{\omega})$ over the frequencies $\tilde{\omega}$. The integral causes all imaginary contributions to vanish, and the structure function is then given by

$$L(k_x, k_y) = \frac{S_0}{\xi_{x0}^2(k_x - k_{x0})^2 + \xi_{y0}^2(k_y - k_{y0})^2 + \xi_{xy0}^2(k_x - k_{x0})(k_y - k_{y0}) + \varepsilon}. \quad (2)$$

Using this two-dimensional fitting function has the advantage that the components of the dominant wave vector of the pattern k_{x0} and k_{y0} and the correlation-length components ξ_{x0} , ξ_{y0} , and ξ_{xy0} are accessible separately.

In the next section we describe the experimental methods used in our experiments. Next, in Sec. III A, we present new data for the temporal behavior of the thermal fluctuations. Then, in Secs. III B and III C, we give a reanalysis of the structure-factor data for several conductivities of I52 that were previously used in Ref. [24]. In Sec. III B we present results for the mean wave vector, and the data for the correlation-length components are given in Sec. III C. Finally, in Sec. IV we summarize our results and give a brief outlook on remaining problems.

II. EXPERIMENTAL METHODS

For the experiments reported here we used the same apparatus and the same NLC cell-assembly technique as described in Ref. [23]. The only difference is that we replaced the light source by a tungsten-halogen light source [40] to obtain better long-time stability of the light intensity. The following steps were taken to prepare the electroconvection cell. First, the NLC I52 was doped with 4.27% by weight of molecular iodine. The mixture was then stored for 28 days at a temperature of about 50 °C. Next, the cell was assembled and filled, obtaining a sample with planar alignment. Finally, the cell was sealed and stored at room temperature for about 8 months [41]. The cell had a thickness of $d = 28 \pm 1 \mu\text{m}$ and, in units of its thickness, had dimensions of $6.4 \times 10^5 : 7.0 \times 10^5 : 1$.

We kept the cell in a state of turbulent convection for about 9 days to allow for a homogeneous distribution of iodine in the cell before starting the experiments. For the different runs we changed the conductivity σ of the NLC by varying the temperature. The conductivity was measured at a frequency of 50 Hz and at a voltage of 2.0 V right before and after an experimental run. Measurements of σ at 64 °C and over a time period of about 400 h showed that the conductivity dropped slowly over time at a rate of $7.2 \times 10^{-11} \Omega^{-1} \text{m}^{-1} \text{day}^{-1}$.

The only difference between the experimental procedures

for results reported in (a) Sec. III A and (b) Secs. III B and III C is as follows. In (a) we took $T = 1024$ single horizontal lines with a width of $X = 256$ pixels and a rate of 30 Hz and assembled them into space-time images for each voltage. In (b) we took 128 images at 10 s intervals with the dimensions of 256×256 pixels for each voltage.

For calibrating the intensity of our shadowgraph signal we took (a) a space-time image for results reported in Sec. III A or (b) 128 images 10 s apart for results reported in Sec. III B without applying a voltage and before starting a run. This was done first with a glass filter [42] inserted into the filter slot of the tungsten-halogen light source and second without a filter. The mean intensity of the averaged images with and without filter was later used for calculating the zero offset of the frame grabber.

After the calibration was done and the conductivity was measured we increased the applied alternating voltage amplitude V in small steps. The alternating voltage had a frequency of 25 Hz. At each V we waited 110 s. During this time we measured V ten times to obtain an average value. Finally we took (a) a space-time image or (b) 128 images 10 s apart.

For results reported in Sec. III A the temperature was 50 °C, which resulted in a conductivity of $\sigma = 5.94 \times 10^{-9} \Omega^{-1} \text{m}^{-1}$. In Sec. III B the temperature and thus the conductivity was changed to investigate the influence of σ on the fluctuations. We used (i) 38 °C, $\sigma = 5.16 \times 10^{-9} \Omega^{-1} \text{m}^{-1}$, (ii) 42 °C, $\sigma = 6.36 \times 10^{-9} \Omega^{-1} \text{m}^{-1}$, (iii) 46 °C, $\sigma = 7.76 \times 10^{-9} \Omega^{-1} \text{m}^{-1}$, (iv) 50 °C, $\sigma = 9.51 \times 10^{-9} \Omega^{-1} \text{m}^{-1}$ (see also Table I in Ref. [24]).

III. EXPERIMENTAL RESULTS

In the next subsection we report on the temporal behavior of the thermal fluctuations, and then in Sec. III B on the dependence of the structure factor on the conductivity.

A. Temporal structure of the fluctuations

Figure 1(a) shows the spatiotemporal evolution of the thermal fluctuations for $\epsilon = -2 \times 10^{-4}$. Each single line is divided by a background line which consists of an average of

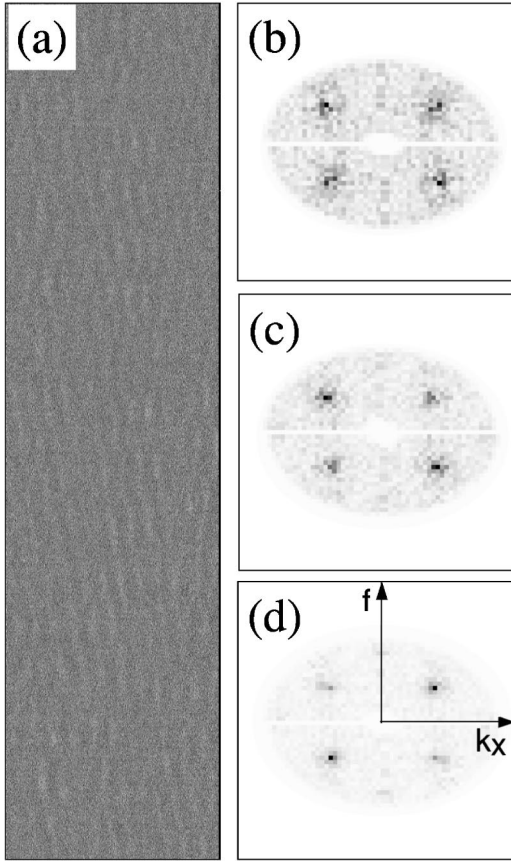


FIG. 1. (a) Spatiotemporal evolution of the thermal fluctuations for $\epsilon = -2 \times 10^{-4}$. The image is background divided. The horizontal axis represents the x axis and is parallel to the director. In this direction the image has a size of $502 \mu\text{m}$. The vertical axis is the time axis. Top is 0 s and bottom is 34.3 s. (b), (c), and (d) are the central parts ($-11.2/d \leq k_x \leq 11.2/d$ and $-14.0 \text{ Hz} \leq f \leq 14.0 \text{ Hz}$) of the Fourier-filtered structure factors $S(k_x, f)$. (b) $\epsilon = -1.25 \times 10^{-2}$; (c) $\epsilon = -2 \times 10^{-4}$; and (d) $\epsilon = 1 \times 10^{-4}$.

all the 1024 lines of the space-time image. Note that in Fig. 1(a) we cannot distinguish between zig and zag modes because only a single line parallel to the director is used. In order to obtain the onset voltage V_c we followed the method described in Refs. [23] and [24] and performed a multimode analysis which was adapted to the space-time images: We calculated $I_i(x, \epsilon) \equiv \tilde{I}_i(x, \epsilon) / \tilde{I}_0(x, \epsilon) - 1$ for each horizontal line $\tilde{I}_i(x, \epsilon)$, $i = 1, \dots, 1024$. Here x is the coordinate in real space parallel to the director, and $\tilde{I}_0(x, \epsilon)$ is a background line obtained by averaging 1024 lines at the same ϵ . For each $I_i(x, \epsilon)$ we derived the structure factor (the square of the modulus of the Fourier transform) $S_i(k_x, \epsilon)$ and averaged 1024 $S_i(k_x, \epsilon)$ to get $S(k_x, \epsilon)$. Here k_x is the wave-vector component in the direction of the director. We computed the total power under the peak of $S(k_x)$ as described in [23], and then converted it to $\langle \theta^2 \rangle$ [43] [see also Eq. (5) in [23]]. Since the primary bifurcation is supercritical the points above onset follow a square-root law. A square-root fit above onset for $134.711 \leq V^2 \leq 135.027 \text{ V}^2$ gave $V_c^2 = 134.6 \text{ V}^2$.

Because the background divided space-time images showed high-frequency noise we applied a filter in Fourier

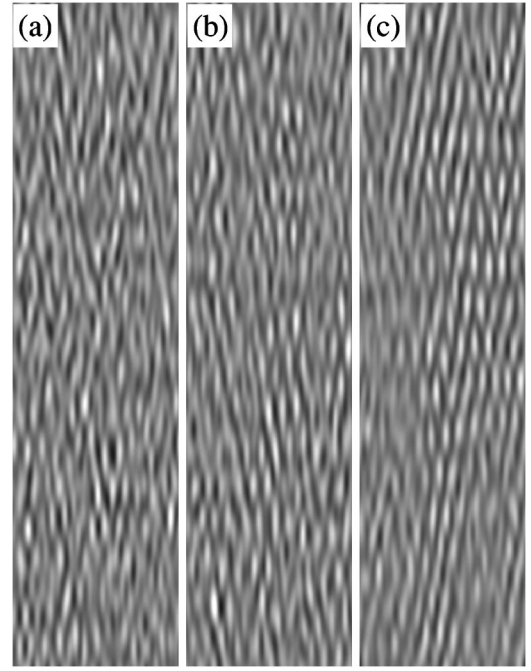


FIG. 2. Spatiotemporal evolution of the right- and left-traveling wave for different ϵ . (a) $\epsilon = -1.25 \times 10^{-2}$; (b) $\epsilon = -2 \times 10^{-4}$; and (c) $\epsilon = 1 \times 10^{-4}$. The images are background divided and Fourier filtered. The horizontal axis represents the x axis and is parallel to the director. In this direction the image has a size of $502 \mu\text{m}$. The vertical axis is the time axis. Top is 0 s and bottom is 34.3 s.

space. This can be seen in Figs. 1(b)–1(d) which show the structure factors $S(k_x, f)$ after applying the Fourier filter and for different values of ϵ . The four main peaks in Figs. 1(b)–1(d) are the two pairs of right- and left-traveling waves.

After applying the filter in Fourier space we transformed the images back to real space. Figures 2(a) and 2(b) show examples below the onset while Fig. 2(c) is an example right above the onset of convection. The two images below the onset do not show much of a difference whereas the image above onset reveals that the right- and left-traveling waves are more ordered. The remaining disorder for $\epsilon > 0$ is due to the spatiotemporal chaos of the pattern. Because the right- and left-TWs are superimposed in these images, we suppressed the right-traveling one in Fourier space, allowing for a better visualization of the left-traveling wave. This is shown in Fig. 3.

For extracting the Hopf frequency ω and the exponential decay time τ we calculated the autostructure function $S_x(\Delta t)$. We chose $S_x(\Delta t)$ instead of the autocorrelation function for reasons discussed in Ref. [44]. The autostructure function is given by

$$S_x(\Delta t) = \sum_{\Delta t=0}^{T/2-1} \frac{1}{X(T-\Delta t)} \times \sum_{i=0}^{X-1} \sum_{t=0}^{T-\Delta t-1} [I(x, t) - I(x, t + \Delta t)]^2, \quad (3)$$

where $X = 256$ is the dimension of the x axis and $T = 1024$ the dimension of the time domain in pixels.

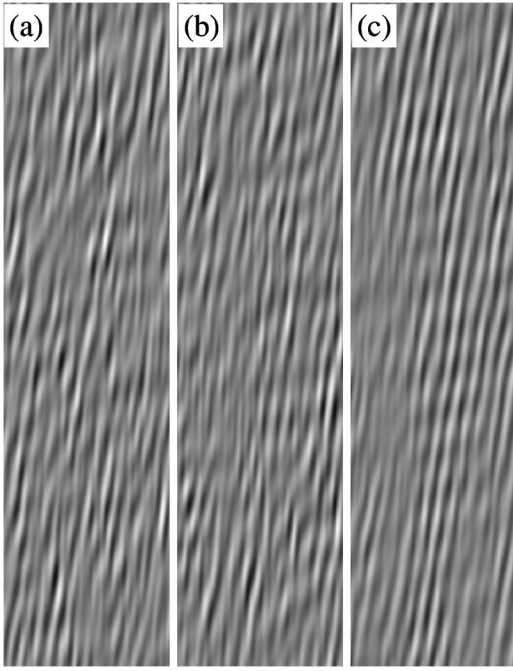


FIG. 3. Spatiotemporal evolution of the left-traveling wave for different ϵ . (a) $\epsilon = -1.25 \times 10^{-2}$; (b) $\epsilon = -2 \times 10^{-4}$; and (c) $\epsilon = 1 \times 10^{-4}$. The images are background divided and Fourier filtered. The right-traveling wave is suppressed in Fourier space. The horizontal axis represents the x axis and is parallel to the director. In this direction the image has a size of $502 \mu\text{m}$. The vertical axis is the time axis. Top is 0 s and bottom is 34.3 s.

In Fig. 4 $S_x(\Delta t)$ is shown for a right-traveling and a left-traveling wave. Fits of the function

$$S_x(\Delta t) = S_x(\infty) [1 - \cos(\omega \Delta t) \exp(-\Delta t / \tau)] \quad (4)$$

to the data are given by the solid lines in the figures. As can be seen, the data for the longer time delays are not described very well by Eq. (4). Most likely the statistics of the runs is not sufficient. Note that the amount of image data at each ϵ is only 1/32 of the amount taken for the results presented in Ref. [24] and in Sec. III B. More work with better statistics would be desirable. Nonetheless, the fits to the $S_x(\Delta t)$ data

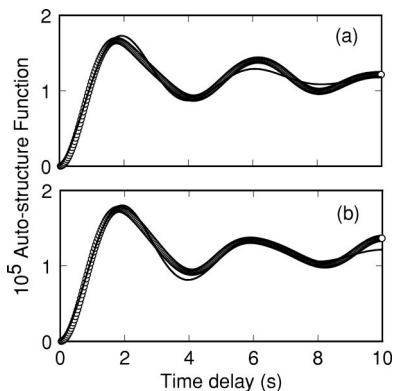


FIG. 4. The autostructure function $S_x(\Delta t)$ for a right-traveling (a) and a left-traveling (b) wave for $\epsilon = -1.25 \times 10^{-2}$. The solid line shows a fit of Eq. (4) to the data (open circles).

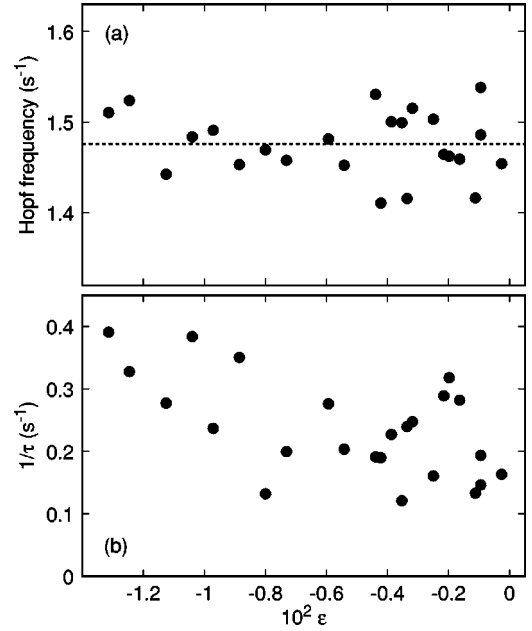


FIG. 5. (a) The Hopf frequency ω as a function of ϵ for measurements below the onset. The dashed line is the average of all data points and gives 1.48 s^{-1} . (b) The inverse of the exponential decay length $1/\tau$ as a function of ϵ for measurements below the onset.

give a good estimate for ω . As can be seen from the figures, the oscillation frequency of the data and the fitted function is essentially the same. The results for τ are not as good; they correspond to the decay rate of the envelope of the oscillations in the figures. However, a semiquantitative estimate is still obtained from the fits.

Both ω and τ are given in Fig. 5 as a function of ϵ . It is seen that ω is constant within our resolution and has an averaged value of 1.48 s^{-1} . According to mean-field theory the inverse of the exponential decay length should go to 0 at $\epsilon_{\text{mf}} = 0$ (or $\epsilon = -4.6 \times 10^{-2}$) as

$$1/\tau = \epsilon / \tau_0. \quad (5)$$

All our data are in the critical region beyond the mean-field onset. There they tend toward a constant value close to 0.2 s^{-1} at $\epsilon = 0$.

Measurements of τ based on the time correlation of fluctuations below onset were made before by Winkler *et al.* [45]. These authors used the NLC MBBA. Their measurements were for $\epsilon \lesssim -0.03$, and in that parameter range they found consistency with linear theory in the sense that their data could be described by Eq. (5). However, the values for τ_0 derived from their data were larger than a theoretical estimate [25] by nearly a factor of 2. So far as we know this disagreement with linear theory remains unexplained.

B. The wave vector of the fluctuations

In this section we present spatially extended and time-averaged results for the fluctuations as a function of the conductivity and of ϵ . We use the same experimental data as presented in Ref. [24] for 152. While Ref. [24] emphasized

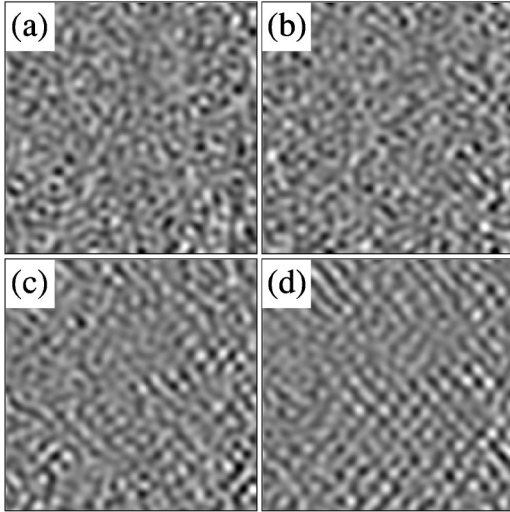


FIG. 6. The background divided and Fourier-filtered snapshots of size $502 \times 502 \mu\text{m}^2$ at $\sigma = 7.8 \times 10^{-9} \Omega^{-1} \text{m}^{-1}$. (a) $\epsilon = -0.320$; (b) $\epsilon = -0.104$; (c) $\epsilon = -0.011$; (d) $\epsilon = -0.001$. The director is horizontal.

the dependence of the mean-square director-angle fluctuations $\langle \theta^2 \rangle$ on ϵ and showed that there are deviations from mean-field theory as the onset of convection is approached, we focus here on the ϵ dependence of the components of the mean wave number and of the correlation length by fitting a two-dimensional Lorentzian function to the structure factors.

Figure 6 shows four examples of single snapshots at different ϵ and for $\sigma = 7.8 \times 10^{-9} \Omega^{-1} \text{m}^{-1}$. Far below onset [Fig. 6(a)] the patterns are very weak. However, dividing by a background image, Fourier filtering, and using the full available gray scale uncovers the expected zig and zag modes. The patches grow as ϵ is increased [Figs. 6(b) and 6(c)]. Very close to onset [Fig. 6(d)] a pattern containing extended patches of zig and zag rolls is found.

For visualizing the structure factors $S(\mathbf{k}, \epsilon)$ [see Figs. 7(a), 7(c), 7(e), and 7(g)], where $\mathbf{k} = (k_x, k_y)$ is the wave vector, we first calculated $I_i(\mathbf{x}, \epsilon) \equiv \tilde{I}_i(\mathbf{x}, \epsilon) / \tilde{I}_0(\mathbf{x}, \epsilon) - 1$ for each image $\tilde{I}_i(\mathbf{x}, \epsilon)$, $i = 1, \dots, 128$. Here $\mathbf{x} = (x, y)$ are the coordinates in real space and $\tilde{I}_0(\mathbf{x}, \epsilon)$ is a background image obtained by averaging 128 images at the same ϵ . For each $I_i(\mathbf{x}, \epsilon)$ we derived the structure factor $S_i(\mathbf{k}, \epsilon)$ (the square of the modulus of the Fourier transform) and averaged 128 $S_i(\mathbf{k}, \epsilon)$ to get $S(\mathbf{k}, \epsilon)$. Figures 7(a), 7(c), 7(e), and 7(g) show two pairs of peaks corresponding to two sets of rolls oriented obliquely to the director which get sharper and larger as we approach the onset of convection. These observations are in agreement with those reported in Refs. [21–23]. The two modes are called zig and zag modes and correspond to those of the extended chaos above onset [27].

Instead of the multimode analysis presented in Ref. [24], we fitted a two-dimensional function

$$S(\mathbf{k}, \epsilon) = L(\mathbf{k}, \epsilon) + B(k_x, \epsilon) \quad (6)$$

to the experimental data for the structure factors. Here $B(k_x, \epsilon)$ is a one-dimensional background function which

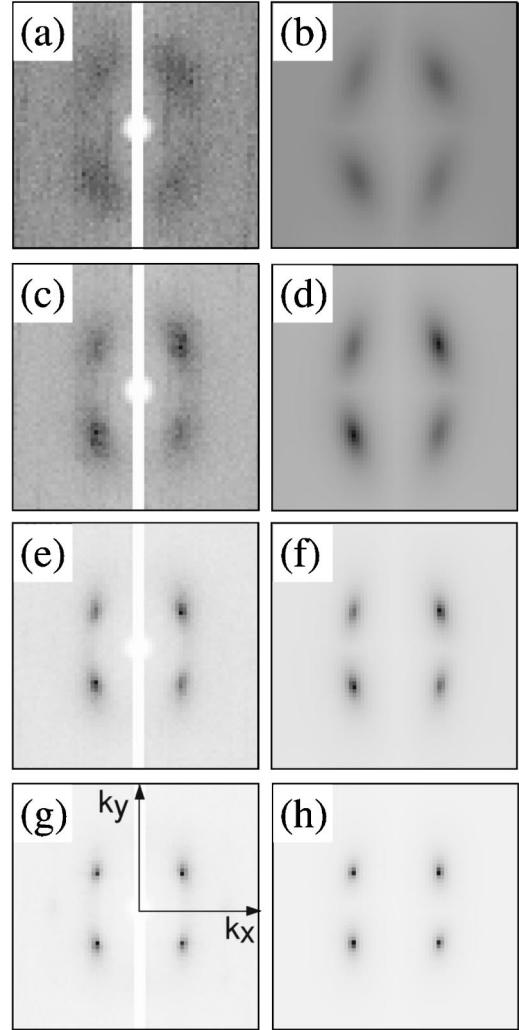


FIG. 7. The central parts $-11.2/d \leq k_x, k_y \leq 11.2/d$ of the time-averaged structure factors $S(\mathbf{k})$ [(a),(c),(e),(g)] and the corresponding visualization of the two-dimensional least-squares fit of Eq. (6) to the data [(b),(d),(f),(h)]. (a),(b) $\epsilon = -0.320$; (c),(d) $\epsilon = -0.104$; (e),(f) $\epsilon = -0.011$; (g),(h) $\epsilon = -0.001$. The director is horizontal.

contains the experimental noise. To a good approximation the background was seen from experiment to increase exponentially with k_x and to be independent of k_y . Thus we chose

$$B(k_x, \epsilon) = a \exp(bk_x), \quad (7)$$

where a and b are fitting parameters that depend only slightly on ϵ . The term $L(\mathbf{k}, \epsilon)$ is the two-dimensional Lorentzian function given by Eq. (2). There S_0/ϵ is the maximum height of the function at the position $\mathbf{k}_0 = (k_{x0}, k_{y0})$ and ξ_{x0}, ξ_{y0} , and ξ_{xy0} are the components of the correlation length. Usually the mean wave number of a pattern is defined as the first moment of the distribution function of the Fourier peak. This is not possible here because Eq. (2) is not integrable and there is no first moment. Thus in the following we refer to \mathbf{k}_0 as the mean wave number. For the purpose of fitting we used

$$L(k_x, k_y) = \frac{\bar{S}_0}{\xi_x^2(k_x - k_{x0})^2 + \xi_y^2(k_y - k_{y0})^2 + \xi_{xy}^2(k_x - k_{x0})(k_y - k_{y0}) + 1} \quad (8)$$

with $\bar{S}_0 = S_0/\epsilon$ and $\xi_n = \xi_{n0}/\epsilon^{1/2}$ for $n = x, y$, and xy .

A two-dimensional nonlinear least-squares fitting routine was used to fit $S(\mathbf{k}, \epsilon) = L(\mathbf{k}, \epsilon) + B(k_x, \epsilon)$ to the experimental data. In Fig. 7 we compare the experimental time-averaged structure factors with the corresponding visualization of the fitting results. The left column shows the experimental data and the right column gives the simulated $S(\mathbf{k}, \epsilon)$. The simulated images of the structure factors agree well with the experimental data. Taking difference images between the experimental and the simulated images did not reveal any significant systematic deviations.

Very close to and above onset our two-dimensional fitting procedure failed because the peaks became too narrow and consisted of only a few pixels. Therefore we chose a different procedure to extract the coordinates $\mathbf{k}_0 = (k_{x0}, k_{y0})$ of the peak. We first detected the maximum value $S_{\max}(\mathbf{k})$ of $S(\mathbf{k})$ in the quadrant $k_x > 0, k_y > 0$ for the zig mode or $k_x > 0, k_y < 0$ for the zag mode and for $B(k_x) < S_{\max}(\mathbf{k})$ (the latter condition was only important for ϵ far below the onset). Next we calculated

$$k_{n0} = \sum S(k_n)k_n / \sum S(k_n), n = x, y, \quad (9)$$

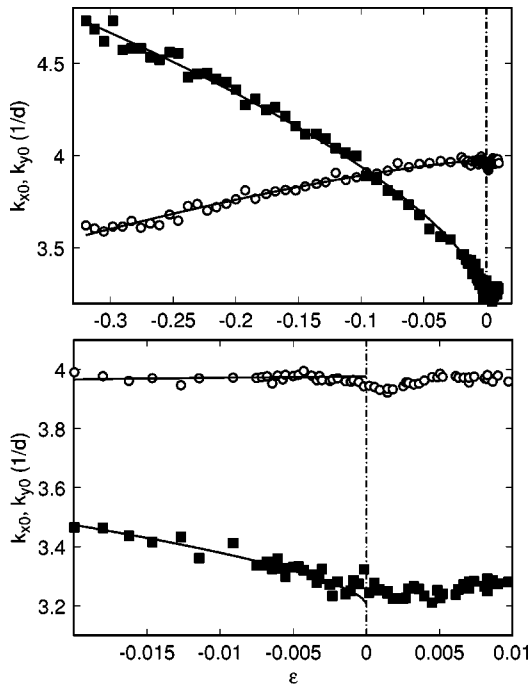


FIG. 8. The components (k_{x0}, k_{y0}) of the mean wave vector \mathbf{k}_0 for $\sigma = 7.8 \times 10^{-9} \Omega^{-1} \text{m}^{-1}$ as a function of ϵ . Open circles: k_{x0} . Solid squares: k_{y0} . The data are averages for the zig and the zag modes. The solid curves are fits to a power law. The lower figure gives an expanded view of the data close to the transition.

where we summed over an area of 9×9 pixels with S_{\max} at the center. Comparing the values for \mathbf{k}_0 as a function of ϵ for the two different methods showed that they are in good agreement for values close to the onset. For values far below the onset there is only a reasonable agreement because here the background is significant and the peaks are much broader than the 9×9 pixels used in the second method. Hence we obtained \mathbf{k}_0 from the second method when the method of fitting the two-dimensional Lorentzian failed, i.e., very close to and above the onset. Unfortunately the second method does not give results for the correlation lengths.

We found within our resolution that the zig and zag modes gave equivalent results for the fitting parameters. Thus, in the following we give only the averages over these two modes. In Fig. 8 we show the coordinates $\mathbf{k}_0 = (k_{x0}, k_{y0})$ of the peak of the fitted Lorentzian function for $\sigma = 7.8 \times 10^{-9} \Omega^{-1} \text{m}^{-1}$ and as a function of ϵ . For ϵ very far from the onset it is seen that k_{x0} is smaller than k_{y0} . For $\epsilon = -0.092$ both components have an equal value. Closer to the onset and above we get $k_{x0} > k_{y0}$.

In the lower part of Fig. 8 the region very close to onset is shown on an expanded horizontal scale. One sees that k_{x0} and k_{y0} are continuous at $\epsilon = 0$, although they seem to have a mild singularity.

An interesting property is the angle of obliqueness ϑ of the rolls, which is defined as $\vartheta = \arctan(k_{y0}/k_{x0})$. First, in Fig. 9, we look at the ratio k_{y0}/k_{x0} as a function of ϵ for $\sigma = 7.8 \times 10^{-9} \Omega^{-1} \text{m}^{-1}$. We fitted the data in three ways. First, a straight line

$$k_{y0}/k_{x0} = a_0(1 + a_1\epsilon) \quad (10)$$

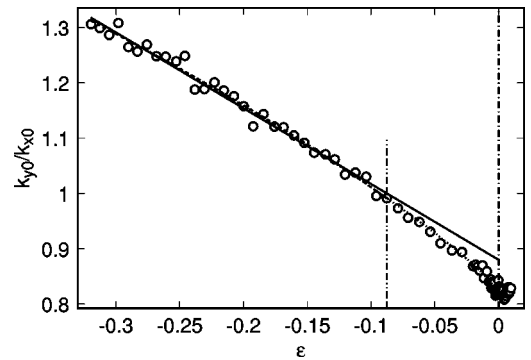


FIG. 9. The ratio between the components of the mean wave vector k_{y0}/k_{x0} for $\sigma = 7.8 \times 10^{-9} \Omega^{-1} \text{m}^{-1}$ as a function of ϵ . The double-dotted double-dashed line at $\epsilon = -8.8 \times 10^{-2}$ gives the upper limit of the region that was used in Fig. 2 of Ref. [24] for fitting in the mean-field region. The solid line is a straight-line fit to the data in the mean-field region, the dashed curve is a power-law fit to the data in the mean-field region, and the dotted line is a power-law fit to the data for $\epsilon < 0$.

TABLE I. Parameters obtained from fits of Eqs. (10) and (11) to the ratio k_{y0}/k_{x0} for different conductivities σ .

$10^9 \sigma$ ($\Omega^{-1} \text{m}^{-1}$)	5.16	6.36	7.76	9.51	Average
a_0	0.866	0.879	0.880	0.868	0.87 ± 0.01
a_1	-1.48	-1.50	-1.56	-1.57	-1.53 ± 0.05
a_2	0.818	0.829	0.820	0.815	0.82 ± 0.01
a_3	1.16	1.20	1.26	1.24	1.22 ± 0.04
a_4	0.834	0.828	0.821	0.819	0.83 ± 0.03

was used in the mean-field region. For the mean-field region we used the same range of ϵ as was used for the fits in Fig. 2 of Ref. [24]. The upper limit of this region is marked by a vertical double-dotted double-dashed line in Fig. 9, and the fit is given as a solid straight line. It yielded $a_0=0.88$ and $a_1=-1.37$. A second fit was a power law

$$k_{y0}/k_{x0} = a_2 + a_3 |\epsilon|^{a_4} \quad (11)$$

for data with $\epsilon < 0$ (dotted line in Fig. 9) and gave $a_2 = 0.82$, $a_3 = 1.26$, and $a_4 = 0.82$. Finally, for comparison we fitted a power law in the mean-field range only (dashed line in Fig. 9) and obtained $k_{y0}/k_{x0} = 0.79 + 1.2 |\epsilon|^{0.73}$. The three fits do not show any significant difference in the mean-field region. However, for values in the critical region the two fitting functions deviate from each other. From a theoretical point of view a straight-line fit is favored in the mean-field region. The deviations of the experimental data from the straight line show that k_{y0}/k_{x0} deviates from LT, i.e., that it is influenced by nonlinear fluctuation interactions; but the good fit obtained with the power law for $\epsilon < 0$ and the resulting exponent remain to be explained.

We performed straight-line fits in the mean-field region and power-law fits for the whole region for four different runs with different conductivities. Table I shows the results a_0, a_1, a_2, a_3 , and a_4 as a function of the conductivity. Within their uncertainties (which are omitted in the table) all five fitting values are independent of σ and can be averaged.

Finally, we present the dependence of the angle of obliqueness on ϵ in Fig. 10. Here we averaged the data of all four different conductivities contained within a window covering an ϵ range $\delta\epsilon = 1.5 \times 10^{-2}$. The two fits, namely, the straight-line fit in the mean-field region and the power-law fit in the whole region, based on parameters in the last column of Table I, are plotted. The fits suggest a critical angle of obliqueness at onset of $\vartheta_c = 0.72$ rad for the extrapolation from the mean-field fit and of $\vartheta_c = 0.69$ rad for the power-law fit.

Next we calculated the modulus of the mean wave vector $k_0 = \sqrt{k_{x0}^2 + k_{y0}^2}$ as a function of ϵ and for different conductivities σ . Unlike the angle of obliqueness, we see in Fig. 11 that k_0 depends on the conductivity, being somewhat larger at lower conductivity. We found that k_0 decreases with increasing ϵ .

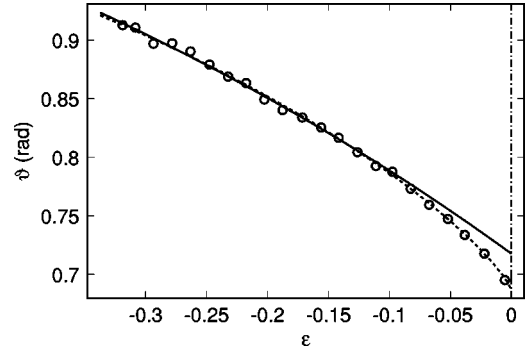


FIG. 10. The angle of obliqueness ϑ as a function of ϵ . Each data point is the result of averaging over all four different conductivities and over a range $\delta\epsilon = 1.5 \times 10^{-2}$.

For fitting the data we followed the approach for fitting the k_{y0}/k_{x0} data: First, we used a straight-line fit in the mean-field region,

$$k_0 = b_0(1 + b_1\epsilon), \quad (12)$$

and second a power-law fit for the whole region of $\epsilon < 0$,

$$k_0 = b_2 + b_3 |\epsilon|^{b_4}. \quad (13)$$

Table II summarizes the results for the fitting parameters for different conductivities. We found that the fitting parameter depends on the conductivity.

C. The correlation length of the fluctuations

From linear theory it is expected that

$$\xi_n = \xi_{n,0}(\epsilon)^{-1/2} \quad (14)$$

with $n=x, y$, or xy . The amplitudes $\xi_{n,0}$ are expected to be regular functions of ϵ , i.e., they should be essentially linear in ϵ .

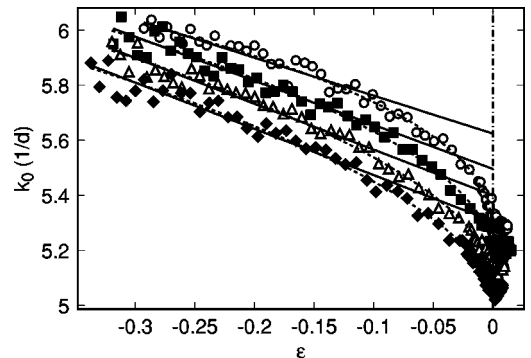


FIG. 11. The modulus of the wave vector k_0 as a function of ϵ and for different conductivities σ . Open circles: $\sigma = 5.2 \times 10^{-9} \Omega^{-1} \text{m}^{-1}$. Solid squares: $\sigma = 6.4 \times 10^{-9} \Omega^{-1} \text{m}^{-1}$. Open triangles: $\sigma = 7.8 \times 10^{-9} \Omega^{-1} \text{m}^{-1}$. Solid diamonds: $\sigma = 9.5 \times 10^{-9} \Omega^{-1} \text{m}^{-1}$. The solid lines are straight-line fits to the data in the mean-field region. The dashed curves are power-law fits to the data for $\epsilon < 0$.

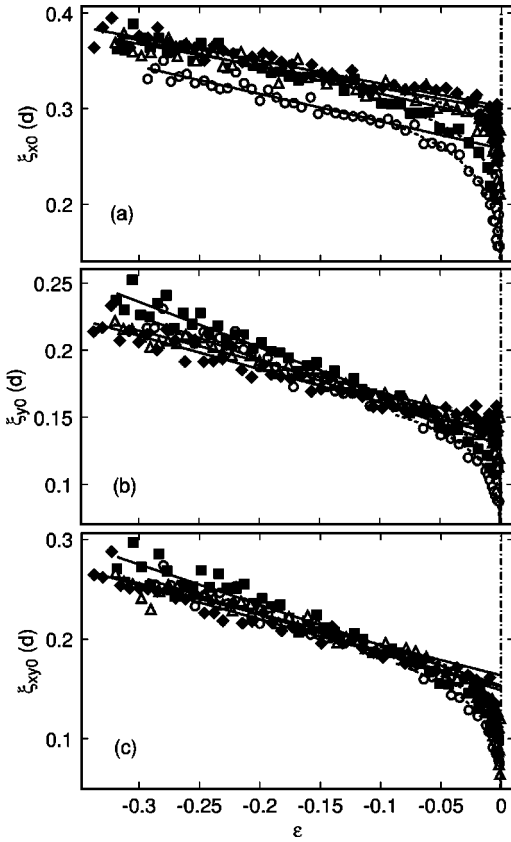


FIG. 12. The amplitudes of the correlation lengths (a) ξ_{x0} , (b) ξ_{y0} , and (c) ξ_{xy0} as functions of ϵ and for different conductivities σ . Open circles: $\sigma = 5.2 \times 10^{-9} \Omega^{-1} \text{m}^{-1}$. Solid squares: $\sigma = 6.4 \times 10^{-9} \Omega^{-1} \text{m}^{-1}$. Open triangles: $\sigma = 7.8 \times 10^{-9} \Omega^{-1} \text{m}^{-1}$. Solid diamonds: $\sigma = 9.5 \times 10^{-9} \Omega^{-1} \text{m}^{-1}$. The solid lines are straight-line fits of the data in the mean-field region. The dashed curves are power-law fits to the data in the critical region.

Fluctuations below onset were used before to study the correlation-length components of EC in NLCs by Hörner and Rehberg [46,21]. These authors investigated the materials MBBA [46] and Merck Phase V [21]. For MBBA in a normal-roll parameter range they found that their data for ξ_x and ξ_y could be described well by Eq. (14) with $\xi_{x,0}$ and $\xi_{y,0}$ independent of ϵ and somewhat smaller than theoretical values based on linear theory [25] (for normal rolls there is no ξ_{xy}). The measurements for Phase V were more detailed [21], and particularly for ξ_x deviations from linear theory were detected near onset, although the interpretation of the

TABLE II. Parameters obtained from fits of Eqs. (12) and (13) to the modulus k_0 of the wave vector for different conductivities σ .

$10^9 \sigma$ ($\Omega^{-1} \text{m}^{-1}$)	5.16	6.36	7.76	9.51
b_0	5.62	5.50	5.40	5.31
b_1	-0.24	-0.29	-0.31	-0.32
b_2	5.24	5.18	5.09	5.02
b_3	1.30	1.47	1.54	1.54
b_4	0.421	0.509	0.540	0.552

TABLE III. Parameters obtained from fitting Eq. (15) to the correlation-length amplitudes in the mean-field region.

10^9 σ ($\Omega^{-1} \text{m}^{-1}$)	5.16	6.36	7.76	9.51
$\xi_{x0}(0)$	0.258	0.288	0.299	0.302
$\xi_{y0}(0)$	0.129	0.134	0.145	0.136
$\xi_{xy0}(0)$	0.149	0.153	0.164	0.152
c_x	-1.11	-0.97	-0.77	-0.79
c_y	-2.48	-2.54	-1.59	-1.83
c_{xy}	-2.55	-2.65	-1.87	-2.24

data apparently assumed that the $\xi_{n,0}$ are ϵ independent over a wide ϵ range.

Here we report our results for I52 which were obtained from the fits of Eq. (8) to the two-dimensional structure factor discussed in the previous section. This fit gives the three correlation-length components ξ_x , ξ_y , and ξ_{xy} . Figure 12 shows the three amplitudes for different conductivities. In the mean-field region they decrease linearly and can be fitted by straight lines:

$$\xi_{n0}(\epsilon) = \xi_{n0}(0)(1 + c_n \epsilon). \quad (15)$$

In Table III the resulting parameters are listed. One sees that ξ_{n0} increases slightly with σ . The absolute values of the coefficients c_n are of order unity, as expected for a regular function of ϵ .

In the critical region the data deviate from the straight lines, and thus from linear theory. There they are better described by a power law:

$$\xi_{n0}(\epsilon) = \xi_{n1}(-\epsilon)^{-(\nu_n - 1/2)}. \quad (16)$$

The parameters obtained from fitting this function to the data are given in Table IV. One sees that ξ_{x1} , ξ_{y1} , and ξ_{xy1} do not depend noticeably on σ , but that the exponents ν_n decrease with increasing conductivities. This is somewhat surprising since exponents are usually universal; but we do not really believe that the data are good enough to unambiguously identify a critical region in which the fit should be carried out and to determine the critical parameters reliably. They do, however, indicate that ν has a value less than its mean-field value 1/2.

TABLE IV. Parameters obtained from fitting Eq. (16) to the correlation-length amplitudes in the critical region.

$10^9 \sigma$ ($\Omega^{-1} \text{m}^{-1}$)	5.16	6.36	7.76	9.51	Average
ξ_{x1}	0.407	0.398	0.374	0.382	0.39 ± 0.04
ξ_{y1}	0.223	0.220	0.171	0.161	0.19 ± 0.04
ξ_{xy1}	0.302	0.283	0.302	0.286	0.29 ± 0.06
ν_x	0.35	0.39	0.43	0.44	—
ν_y	0.34	0.37	0.46	0.32	—
ν_{xy}	0.28	0.32	0.32	0.34	—

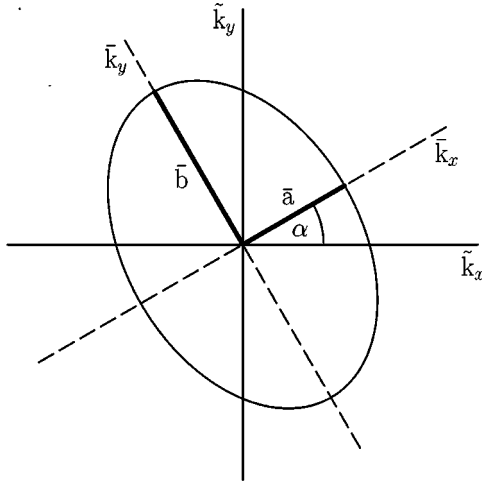


FIG. 13. Illustration of the coordinate transformation $\tilde{\mathbf{k}} \rightarrow \bar{\mathbf{k}}$. The rotation angle is given by α . The ellipse is a result of a cut through the Lorentzian peak parallel to the (k_x, k_y) plane at the height of $S(\mathbf{k}) = S(k_{x0}, k_{y0})/2$.

A cut through the structure factors [see, e.g., Fig. 7] parallel to the (k_x, k_y) plane yields an elliptical area. However, due to the cross term $\xi_{xy}^2(k_x - k_{x0})(k_y - k_{y0})$ in the denominator of Eq. (8) the two axes of the ellipse are not parallel to the k_x and k_y axes. In order to study the angle of inclination α of the ellipse, we shifted the origin to the center of the peak, yielding new coordinates $(\tilde{k}_x, \tilde{k}_y)$. Then we carried out a rotation through an angle α so as to align the axes of the coordinate system with the axes of the ellipse, yielding coordinates (\bar{k}_x, \bar{k}_y) . This alignment is achieved when the cross

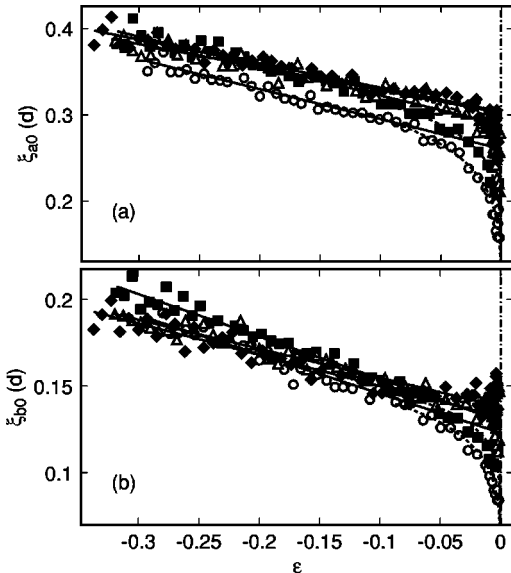


FIG. 14. The amplitude of the transformed correlation lengths (a) ξ_{a0} and (b) ξ_{b0} as a function of ϵ and for different conductivities σ . Open circles: $\sigma = 5.2 \times 10^{-9} \Omega^{-1} \text{m}^{-1}$. Solid squares: $\sigma = 6.4 \times 10^{-9} \Omega^{-1} \text{m}^{-1}$. Open triangles: $\sigma = 7.8 \times 10^{-9} \Omega^{-1} \text{m}^{-1}$. Solid diamonds: $\sigma = 9.5 \times 10^{-9} \Omega^{-1} \text{m}^{-1}$. The solid lines are straight-line fits to the data in the mean-field region. The dashed curves are power-law fits to the data in the critical region.

TABLE V. Parameters obtained from fitting an equation like Eq. (15) to the correlation-length amplitudes ξ_{a0} and ξ_{b0} in the mean-field region.

$10^9 \sigma$ ($\Omega^{-1} \text{m}^{-1}$)	5.16	6.36	7.76	9.51
$\xi_{a0}(0)$	0.260	0.288	0.302	0.304
$\xi_{b0}(0)$	0.123	0.130	0.138	0.132
c_a	-1.33	-1.18	-0.88	-0.91
c_b	-1.84	-1.88	-1.22	-1.36

term vanishes. The transformation is illustrated in Fig. 13.

In polar coordinates (r, ϕ) one now has

$$L(r, \phi - \alpha) = \frac{\tilde{S}_0}{\xi_a^2 r^2 \cos^2(\phi - \alpha) + \xi_b^2 r^2 \sin^2(\phi - \alpha) + 1} \quad (17)$$

for the Lorentzian function. As seen in Fig. 13, \bar{a} and \bar{b} now denote the axes of the ellipse. For $L(\bar{k}_x, \bar{k}_y) = \tilde{S}_0/2$ one has $\bar{a} = 1/\xi_a$ and $\bar{b} = 1/\xi_b$. For ξ_a , ξ_b , and α one obtains

$$\xi_{a,b} = (1/2) [\xi_x^2 + \xi_y^2 \pm \sqrt{(\xi_x^2 - \xi_y^2)^2 + \xi_{xy}^4}] \quad (18)$$

and

$$\alpha_{1,2} = \arctan \left[\frac{\xi_y^2 - \xi_x^2}{\xi_{xy}^2} \pm \sqrt{\frac{(\xi_x^2 - \xi_y^2)^2}{\xi_{xy}^4} + 1} \right]. \quad (19)$$

The angle α_1 (α_2) aligns the \tilde{k}_x (\tilde{k}_y) axis with the \bar{a} axis of the ellipse (see Fig. 13). In the following we chose $\alpha = \alpha_1$ as our rotation axis.

The Lorentzian function Eq. (17) now contains three transformed parameters, namely, the correlation lengths ξ_a and ξ_b and the rotation angle α . The correlation-length amplitudes $\xi_{a0} = \xi_a(-\epsilon)^{1/2}$ and $\xi_{b0} = \xi_b(-\epsilon)^{1/2}$ are shown in Fig. 14 as a function of ϵ . As one would expect, we find behavior similar to that of the amplitudes ξ_{x0} , ξ_{y0} , and ξ_{xy0} . In the mean-field region ξ_{a0} and ξ_{b0} decrease linearly with increasing ϵ . In the critical region the data can be described by a power law. Tables V and VI show the dependences of the fitting parameters on the conductivity.

Figure 15 illustrates the dependence of the rotation angle α on ϵ and σ . We note that α and the angle of obliqueness ϑ of the rolls (see Fig. 10) are two unrelated quantities. Indeed,

TABLE VI. Parameters obtained from fitting an equation like Eq. (16) to the correlation-length amplitudes ξ_{a0} and ξ_{b0} in the critical region.

$10^9 \sigma$ ($\Omega^{-1} \text{m}^{-1}$)	5.16	6.36	7.76	9.51	Average
ξ_{a1}	0.423	0.410	0.386	0.390	0.40 ± 0.04
ξ_{b1}	0.199	0.186	0.154	0.146	0.17 ± 0.04
ν_a	0.34	0.38	0.43	0.44	
ν_b	0.36	0.40	0.48	0.50	

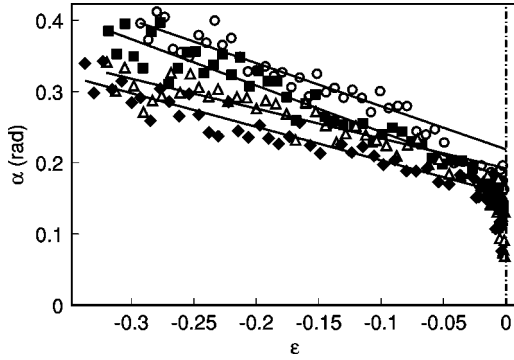


FIG. 15. The rotation angle α as a function of ϵ and for different conductivities σ . Open circles: $\sigma = 5.2 \times 10^{-9} \Omega^{-1} \text{m}^{-1}$. Solid squares: $\sigma = 6.4 \times 10^{-9} \Omega^{-1} \text{m}^{-1}$. Open triangles: $\sigma = 7.8 \times 10^{-9} \Omega^{-1} \text{m}^{-1}$. Solid diamonds: $\sigma = 9.5 \times 10^{-9} \Omega^{-1} \text{m}^{-1}$. The solid lines are straight-line fits to the data in the mean-field region.

α is much smaller than ϑ over the entire ϵ range. One sees that α decreases slightly with increasing σ . The rotation angle decreases linearly with increasing ϵ in the mean-field region and also somewhat closer to onset. For $\epsilon \leq 0.01$ α seems to decrease precipitously, perhaps toward zero at $\epsilon = 0$; but we do not have the resolution to determine the behavior very close to onset with certainty. We note also that the determination of α becomes more difficult at small ϵ since the Lorentzian peak becomes more narrow. We fitted a straight line

$$\alpha = d_0(1 + d_1\epsilon) \quad (20)$$

to the data in the mean-field region for different conductivities and give the parameters in Table VII.

Another property to look at is the eccentricity of the ellipse as a function of ϵ and σ . It is defined as

$$e = \sqrt{1 - \bar{a}^2/\bar{b}^2} = \sqrt{1 - \xi_b^2/\xi_a^2}. \quad (21)$$

Figure 16 gives the dependence of e on ϵ and σ . We observe that e increases with increasing ϵ in the mean-field region where a straight line

$$e = e_0(1 + e_1\epsilon) \quad (22)$$

describes the data (see Table VIII for values of e_0 and e_1). This means that the ellipse becomes more elliptic as we increase ϵ in the mean-field region. However, as we get closer to the onset the value of e drops, i.e., the ellipse becomes more circular although the eccentricity remains pronounced.

TABLE VII. Parameters obtained by fitting Eq. (20) to the data for the rotation angle α in the mean-field region.

$10^9 \sigma$ ($\Omega^{-1} \text{m}^{-1}$)	5.16	6.36	7.76	9.51
d_0 (rad)	0.219	0.178	0.192	0.156
d_1	-2.76	-3.66	-2.19	-3.02

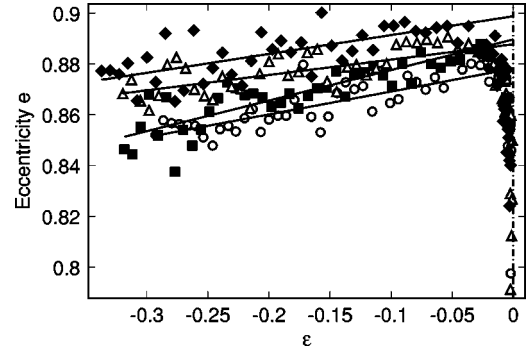


FIG. 16. The eccentricity e as a function of ϵ and for different conductivities σ . Open circles: $\sigma = 5.2 \times 10^{-9} \Omega^{-1} \text{m}^{-1}$. Solid squares: $\sigma = 6.4 \times 10^{-9} \Omega^{-1} \text{m}^{-1}$. Open triangles: $\sigma = 7.8 \times 10^{-9} \Omega^{-1} \text{m}^{-1}$. Solid diamonds: $\sigma = 9.5 \times 10^{-9} \Omega^{-1} \text{m}^{-1}$. The solid lines are straight-line fits to the data in the mean-field region.

IV. SUMMARY AND OUTLOOK

We presented two different sets of measurements. The first consisted of an experimental run at an intermediate conductivity where the primary bifurcation to electroconvection is supercritical. The temporal behavior of thermal fluctuations below the onset but only in the critical region was investigated by taking and analyzing space-time images. The space coordinate was parallel to the director. Within our resolution the Hopf frequency ω was independent on ϵ and had a value of 1.48 s^{-1} . The correlation time τ was determined only semiquantitatively because data with adequate statistics could not be obtained within the scope of this work. However, it appears that $1/\tau$ remains finite at $\epsilon = 0$, contrary to expectations based on LT.

The second set of measurements consisted of the I52 data presented in Ref. [24], where images of the fluctuations far below and very close to onset were taken for four different conductivities covering a wide range of σ over which the primary bifurcation to electroconvection is supercritical. In Ref. [24], the focus was on the mean-square director-angle fluctuations, and it was demonstrated that there are deviations from LT as the onset is approached. Here we analyzed the components of the mean wave vector and the correlation length. To do so we used a two-dimensional Lorentzian function to fit the data, instead of fitting a one-dimensional Lorentzian function to the azimuthally averaged structure factors as was done before [22,23].

We showed that the ratio k_{y0}/k_{x0} of the wave vector components is a linear function of ϵ in the mean-field region. In the critical region there are deviations from the straight line, and a power law provides an excellent fit for all the data. The

TABLE VIII. Parameters obtained by fitting Eq. (22) to the data for the eccentricity e in the mean-field region.

$10^9 \sigma$ ($\Omega^{-1} \text{m}^{-1}$)	5.16	6.36	7.76	9.51
e_0 (rad)	0.878	0.890	0.888	0.899
e_1	0.10	0.13	0.07	0.08

angle of obliqueness of the rolls is given by $\vartheta = \tan^{-1}(k_{y0}/k_{x0})$. Well below onset, near $\epsilon = -0.3$, it is as large as 52° . It decreases as the onset is approached, and close to onset is near 40° . We also found that ϑ is independent of σ . The modulus k_0 of the wave vector decreased linearly with increasing ϵ in the mean-field region, and decreased more rapidly in the critical zone. The modulus decreased mildly with increasing σ .

With increasing ϵ the three amplitudes ξ_{x0} , ξ_{y0} , and ξ_{xy0} of the correlation length decreased linearly in the mean-field region and more rapidly in the critical region. In the critical region a power law provided an excellent fit. The amplitudes of the correlation lengths vary only slightly with σ .

The cross section of the structure factor parallel to the $k_x - k_y$ plane has an elliptical shape. The minor (major) axis \bar{a} (\bar{b}) of the ellipse is rotated relative to the k_y (k_x) axis by an angle α . We determined the correlation lengths ξ_a and ξ_b in the direction of the \bar{a} and \bar{b} axes, as well as the angle α . As expected, the behavior of ξ_a and ξ_b was qualitatively similar to that of ξ_x and ξ_y . The angle α was near 17° , i.e., much smaller than the angle of obliqueness ϑ . It decreased slightly with increasing ϵ . We also determined the eccentricity of the ellipse and found it to increase very slightly in the mean-field region but to decrease rapidly in the critical region. The angle α and the eccentricity depend slightly on the conductivity.

In summary, we found the following scenario for the Fourier peak as the onset to electroconvection is approached:

The center of the peak shifts from a larger to a smaller angle of obliqueness and the wavelength of the pattern becomes larger. More subtle is the fact that the tilt of the Fourier peak becomes smaller and the eccentricity of its cross section becomes larger in the mean-field region; but both drop in the critical zone.

Finally, we remark that much remains to be done in the study of nonlinear fluctuations in EC. From the theoretical viewpoint it would be useful to obtain quantitative data for a system with a stationary bifurcation. In that case the usual renormalization-group methods, which assume the existence of a potential for the deterministic system, would be more readily applicable. In order to explore the richness of phenomena that occur in these systems, it would be desirable to study systems with different symmetries. Obvious candidates are oblique and normal rolls, that may belong to different universality classes. The crossover from one to the other, in the vicinity of a Lifshitz point, would be particularly interesting.

ACKNOWLEDGMENTS

This work was supported by National Science Foundation Grant No. DMR00-71328. We owe much to W. Pesch for many helpful discussions. M.A.S. gratefully acknowledges support from the Alexander von Humboldt Foundation. G.A. is thankful for support by NATO Linkage Grant No. CR-G.LG.973103.

-
- [1] For a variety of different examples, see P. Ball, *The Self-Made Tapestry: Pattern Formation in Nature* (Oxford University Press, Oxford, 1999).
- [2] A. Sornberger and M. Parry, *Phys. Rev. D* **62**, 083511 (2000).
- [3] For a comprehensive review, see M.C. Cross and P.C. Hohenberg, *Rev. Mod. Phys.* **65**, 851 (1993).
- [4] C.W. Meyer, G. Ahlers, and D.S. Cannell, *Phys. Rev. Lett.* **59**, 1577 (1987); G. Ahlers, C.W. Meyer, and D.S. Cannell, *J. Stat. Phys.* **54**, 1121 (1989).
- [5] I. Rehberg, S. Rasenat, M. de la Torre-Juarez, W. Schöpf, F. Hörner, G. Ahlers, and H.R. Brand, *Phys. Rev. Lett.* **67**, 596 (1991).
- [6] For a review, see E. Bodenschatz, W. Pesch, and G. Ahlers, *Annu. Rev. Fluid Mech.* **32**, 709 (2000).
- [7] By linear theory (LT) we mean that the nonlinear terms in the equations of motion (e.g., in the Boussinesq equations for RBC, see Ref. [6]) are neglected. As pointed out by J.V. Sengers (private communication), even in LT the stochastic terms in fluctuating hydrodynamics lead to mode coupling; but they do not lead to nonlinear saturation as the onset is approached from below.
- [8] V.M. Zaitsev and M.I. Shliomis, *Zh. Éksp. Teor. Fiz.* **59**, 1583 (1970) [*Sov. Phys. JETP* **32**, 866 (1971)].
- [9] R. Graham, *Phys. Rev. A* **10**, 1762 (1974).
- [10] See R. Graham, in *Fluctuations, Instabilities, and Phase Transitions*, Vol. 11 of *NATO Advanced Study Institute, Series B: Physics*, edited by T. Riste (Plenum, New York, 1975), Sec. 4.2.
- [11] J. Swift and P.C. Hohenberg, *Phys. Rev. A* **15**, 319 (1977).
- [12] P.C. Hohenberg and J.B. Swift, *Phys. Rev. A* **46**, 4773 (1992).
- [13] L.D. Landau and E.M. Lifshitz, *Fluid Mechanics* (Addison-Wesley, Reading, MA, 1959).
- [14] H. van Beijeren and E.G.D. Cohen, *J. Stat. Phys.* **53**, 77 (1988).
- [15] J.M. Ortiz de Zárate and J.V. Sengers, *Physica A* **300**, 25 (2001); and (unpublished).
- [16] G. Quentin and I. Rehberg, *Phys. Rev. Lett.* **74**, 1578 (1995).
- [17] M. Wu, G. Ahlers, and D.S. Cannell, *Phys. Rev. Lett.* **75**, 1743 (1995).
- [18] For a discussion of these results, see also Ref. [6].
- [19] The effective noise intensity F , and thus the critical region, becomes large for RBC of a fluid near a liquid-gas critical point because small cell spacings can be used and because the thermal diffusivity (which enters into F) becomes small [see Eqs. (2.17) and (3.12c) of Ref. [12]]. This was noted also by M. Assenheimer and V. Steinberg, *Europhys. News* **27**, 143 (1996).
- [20] For a review of pattern formation in liquid crystals, see L. Kramer and W. Pesch, *Annu. Rev. Fluid Mech.* **27**, 515 (1995); W. Pesch and U. Behn, in *Evolution of Spontaneous Structures in Dissipative Continuous Systems*, Lecture Notes in Physics Vol. M55, edited by F.H. Busse and S.C. Müller (Springer, New York, 1998).

- [21] F.-D. Hörner, Ph.D. thesis, Universität Bayreuth, Bayreuth, Germany, 1996.
- [22] U. Bisang and G. Ahlers, Phys. Rev. Lett. **80**, 3061 (1998).
- [23] U. Bisang and G. Ahlers, Phys. Rev. E **60**, 3910 (1999).
- [24] M.A. Scherer, G. Ahlers, F. Hörner, and I. Rehberg, Phys. Rev. Lett. **85**, 3754 (2000).
- [25] E. Bodenschatz, W. Zimmermann, and L. Kramer, J. Phys. (France) **49**, 1875 (1988).
- [26] M. Dennin, D.S. Cannell, and G. Ahlers, Phys. Rev. E **57**, 638 (1998).
- [27] M. Dennin, G. Ahlers, and D.S. Cannell, Phys. Rev. Lett. **77**, 2475 (1996).
- [28] M. Dennin, G. Ahlers, and D.S. Cannell, Science **272**, 388 (1996).
- [29] For wave vectors very different from the critical wave vectors and for large ϵ , corrections are expected which will remove the ultraviolet divergence of the integral of Eq. (2) (for the RBC analog, see, for instance, Ref. [15]). For our work Eq. (2) is expected to be an excellent approximation.
- [30] M. Dennin, Phys. Rev. E **62**, 6780 (2000).
- [31] S. Kai and K. Hirakawa, Prog. Theor. Phys. Suppl. **64**, 212 (1978).
- [32] A. Joets and R. Ribotta, Phys. Rev. Lett. **60**, 2164 (1988).
- [33] I. Rehberg, S. Rasenat, and V. Steinberg, Phys. Rev. Lett. **62**, 756 (1989).
- [34] I. Rehberg, S. Rasenat, M. de la Torre Juárez, and V. Steinberg, Phys. Rev. Lett. **61**, 2449 (1988).
- [35] M. Dennin, G. Ahlers, and D.S. Cannell, in *Spatio-Temporal Patterns*, edited by P.E. Cladis and P. Muhoray (Addison-Wesley, Reading, MA, 1994), p. 353.
- [36] M. Dennin, D.S. Cannell, and G. Ahlers, Mol. Cryst. Liq. Cryst. Sci. Technol., Sect. A **261**, 377 (1995).
- [37] M. Treiber and L. Kramer, Mol. Cryst. Liq. Cryst. Sci. Technol., Sect. A **261**, 311 (1995).
- [38] M. Dennin, M. Treiber, L. Kramer, G. Ahlers, and D.S. Cannell, Phys. Rev. Lett. **76**, 319 (1996).
- [39] M. Treiber, N. Éber, Á. Buka, and L. Kramer, J. Phys. II **7**, 649 (1997).
- [40] The light source (model LS-1-LL) was provided by Ocean Optics, Inc., 380 Main Street, Dunedin, FL 34698.
- [41] A second cell, which was filled with the same material about 9 months after the doping of the NLC showed the same patterns at onset and the same values of conductivities.
- [42] As a filter we used a single glass slide (Corning Micro Slides Plain) as provided by Corning Glass Works, Corning, NY 14830.
- [43] S. Rasenat, G. Hartung, B.L. Winkler, and I. Rehberg, Exp. Fluids **7**, 412 (1989).
- [44] E.O. Schulz-DuBois and I. Rehberg, Appl. Phys. **24**, 323 (1981).
- [45] B.L. Winkler, W. Decker, H. Richter, and I. Rehberg, Physica D **61**, 284 (1992).
- [46] F. Hörner and I. Rehberg, in *Pattern Formation in Complex Dissipative Systems*, edited by S. Kai (World Scientific, Singapore, 1992).